

**Title: Behavioral and neural bases of tactile shape discrimination learning in head-fixed mice**

Jinho Kim<sup>1</sup>, Jonathan A. Cheung<sup>1,2</sup>, Samuel Andrew Hires<sup>1,\*</sup>

<sup>1</sup>Department of Biological Sciences, Section of Neurobiology, University of Southern California, Los Angeles, CA 90089, USA

<sup>2</sup>Neuroscience Graduate Program, University of Southern California, Los Angeles, CA 90089, USA

\*Lead contact: shires@usc.edu

**Summary:**

A primary component of tactile shape recognition is perception of the local angle of object surfaces. We investigated how object-angle perception is learned at behavioral and neural levels. We trained head-fixed mice to discriminate object angles by active exploration with one whisker. Three-dimensional whisker analysis of twelve tactile features showed that vertical bending and slide distance were the most important for fine object-angle discrimination. We mapped object-angle tuning of excitatory neurons in layers 2-4 of barrel cortex across learning with calcium imaging. Vertical bending and slide distance also best explained object-angle tuning. Only 40% of recorded neurons were active in both naive and expert sessions. Despite this active ensemble turnover, the population distribution of angle-tuning preferences remained stable. Persistent angle-tuned neurons maintained tuning properties, while recruited ensemble members had sharper tuning compared to lost members. These results show how sensory discrimination training improves representational efficiency while maintaining perceptual stability.

## Introduction

Tactile recognition of the three-dimensional shape of objects is essential for skilled interactions with the world. Whether with hands (Gibson, 1962) or with whiskers (Carvell and Simons, 1990), active tactile shape perception involves purposely scanning an object in search of tactile features relevant for recognizing object identity (Katz, 1925). Over a century of work has yielded tremendous knowledge of the sampling strategies used to gather tactile information (Cheung et al., 2019; Harvey et al., 2001; Lederman and Klatzky, 1987; Mehta et al., 2007; Roland and Mortensen, 1987; Vincent, 1912), how tactile information is transduced by mechanoreceptors in primary sensory afferents (Adrian and Zotterman, 1926; Coste et al., 2012; Hensel and Boman, 1960; Iggo, 1962; McCarter et al., 1999; Werner and Mountcastle, 1965; Zucker and Welker, 1969), where classes of tactile information (e.g. orientation, vibration, texture) are segregated (Gardner and Palmer, 1989; Li et al., 2011; Phillips and Johnson, 1981; Shipley, 1974; Usoskin et al., 2015; Vallbo and Johansson, 1984) and hierarchically combined across ascending and cortical brain regions (Bensmaia et al., 2008; Fitzgerald et al., 2004; Petersen et al., 2008; Pruszynski and Johansson, 2014; Pubols and Leroy, 1977; Sakurai et al., 2013). Much less is known about the fine-scale structure of cortical representations of shape and shape-relevant tactile features (Peron et al., 2015). Moreover, details of how these representations reorganize during shape discrimination learning are virtually unknown, due to inability to make densely sampled, spatially resolved, chronic neuronal recordings in cortex of behaving primates and humans.

Cortical representations of tactile features and object shape are well-suited for study in the rodent whisker system. Rodents can be trained to perform active tactile tasks under head-fixation (Harvey et al., 2001; O'Connor et al., 2010; Sofroniew et al., 2015), where whisker exploration (whisking) is similar to the freely-moving state (Hill et al., 2008). Whiskers are external, so the sensory features driving mechanoreceptor activity in the follicle can be optically quantified (Bagdasarian et al., 2013; Clack et al., 2012; Huet et al., 2015; Pammer et al., 2013). This is critical for relating tactile features to neuronal activity. Whisker primary somatosensory cortex (*i.e.*, barrel cortex, S1) is organized with a one-to-one mapping between whisker and

cortical column in thalamo-cortical recipient layer 4 (Welker, 1971; Woolsey and Van der Loos, 1970). This allows targeting of touch-relevant cortical activity. Genetically-engineered mice (Luo et al., 2008) can express calcium indicators in specific neuronal cell-types (Chen et al., 2013; Horikawa et al., 2010; Wekselblatt et al., 2016). This allows dense, chronic tracking of activity patterns in thousands of neurons per animal across learning (Chen et al., 2015; Madisen et al., 2015; Peron et al., 2015; Wekselblatt et al., 2016). These advantages have facilitated mapping of representations of whisker touch and motion (Peron et al., 2015), touch timing (Hires et al., 2015), object location (Pluta et al., 2017; Ranganathan et al., 2018), and surface texture (Chen et al., 2015; von Heimendahl et al., 2007; Isett et al., 2018) in defined neuronal cell-types of barrel cortex during active tactile behavior. The same advantages apply to investigation of neuronal representations of object shape.

A primary component of tactile shape recognition is perception of the local angle of object surfaces. Many tactile features could plausibly be used to discriminate local object angle and generate angle-specific neural activity in mice. Primary sensory afferents respond to multiple aspects of whisking and active touch including whisking phase (Severson et al., 2017; Wallach et al., 2016), position and velocity (Bale et al., 2013), extrinsic muscular stress (Severson et al., 2017), touch direction (Zucker and Welker, 1969), touch onset, duration and offset (Szwed et al., 2003, 2006), position of the whisker at touch (Szwed et al., 2003), radial distance of the contact point (Szwed et al., 2006), vibration (Arabzadeh et al., 2005), and forces and bending moments during touch (Bush et al., 2016; Campagner et al., 2016). Understanding shape perception requires identifying the extent to which such sensorimotor features affect object-angle discrimination and its central representations.

Sensory discrimination performance can be improved through training (Gibson, 1963; James, 1890). Reorganization of activity in primary sensory cortices may underlie improved performance, as cortical circuits are highly plastic (Calford, 2002; Holtmaat and Svoboda, 2009; LeMessurier and Feldman, 2018; LeMessurier et al., 2019; Margolis et al., 2012; Weinberger, 1995) and combine bottom-up sensory signals with top-down modulatory signals that can instruct plasticity (Aronoff et al., 2010; Cauller, 1995; Gilbert and Li, 2013; Makino and Komiyama, 2015; Manita et al., 2015; White and DeAmicis, 1977; Zhang et al., 2014). However,

reorganization of sensory cortical activity is constrained by a need to maintain perceptual stability (Clopath et al., 2017; Druckmann and Chklovskii, 2012; Lütcke et al., 2013). Whether sensory discrimination learning leads to reshaping neuronal activity selective to trained sensory stimuli in primary sensory cortex remains controversial (Chen et al., 2015; Clopath et al., 2017; Ghose et al., 2002; Jurjut et al., 2017; Peron et al., 2015; Poort et al., 2015; Schoups et al., 2001).

To understand how learned shape recognition is accomplished at behavioral and neural levels, we tracked whisker-object interactions and the resulting neural activity patterns in layers 2-4 of primary somatosensory cortex (S1) across training in a local object-angle discrimination task. We identified the sensorimotor features that best discriminate object angle and choice, mapped tactile features and object-angle related activity patterns in S1, and showed how neuronal preferences for particular tactile features establish the observed patterns of object-angle tuning. Across learning, we saw dramatic reorganization of active ensemble membership during task performance, but a remarkable stability in ensemble tuning. This reflected two factors: a replacement of less selective members with similarly tuned, but more selective members in the expert state, and a persistent group of object-angle tuned neurons that maintained tuning preference and strength between naive and expert states. Beyond producing the first fine-scale map of the evolution of local shape representation in S1, these results reveal how reorganization of neural activity patterns during learning can improve representational efficiency while maintaining stability of sensory perception.

## Results

### *Mice can discriminate object angle with one whisker*

To investigate the sensorimotor basis of object-angle perception, we developed a novel lick left/right active whisker-guided object-angle discrimination task. We trained water-restricted head-fixed mice (n=12) to use a single whisker to discriminate the angle of a smooth pole, randomly presented at different angles (45-135° from the horizontal plane) on an anteroposterior axis beside the face (**Figures 1A and S1A**). Water rewards were available on the right port for 45-75°, the left port for 105-135°, and randomly for 90° (*i.e.* vertical). The anteroposterior location of the pole was jittered (0-2 mm) every trial so that object presence at a particular elevation and location could not be used to consistently discriminate angle. Mice were trimmed to a single whisker C2 at least one week before start of the two-photon imaging (C2 barrel column identification) and throughout training till task mastery. During auditory-cued pole presentation, mice actively whisked into and along the pole during contiguous sampling and answer periods (**Figure S1A**). Training proceeded through stages of increasing difficulty based on the rate of progress of each mouse (**Figure S1B**). To facilitate learning, training was done using 2 angles only (45° and 135°). Six of 12 mice reached our expert performer criteria of 75% correct across 3 consecutive sessions of 2-angle discrimination (45 vs. 135°) in  $14.2 \pm 1.9$  training sessions (**Figure 1B**). Licking became highly stereotyped within approximately three sessions in both learners and non-learners, long before task mastery was achieved (**Figure S2**). This indicates that operant aspects of the task were learned prior to achieving high sensory discrimination performance.

To study finer object-angle discrimination, we tested mice with 7 angles before and after learning (naive 7-angle session, expert 7-angle session, respectively). Following task acclimation, but before learning (*i.e.* naive), these mice performed at chance when discriminating 7 angles (**Figure 1C**). After reaching expert, they performed at  $85.8 \pm 1.2$  % for 2-angle and  $70.0 \pm 2.7$  % for 7-angle discrimination. At this stage, jittering the radial distance of the pole from the face (0-5 mm) showed no significant impact on 2-angle discrimination performance (radial jitter session; **Figures 1C and S1B**). Finally, trimming the whisker caused

performance to fall to chance in all mice across 3 days of further training, indicating that mice relied on whisker tactile stimuli to solve the task (**Figure 1C**).

Prior to training, mice showed varying levels of lick side bias, but no ability to discriminate angle (**Figure 1D**). Following training, expert mice showed a monotonic relationship between licking left and object angle (**Figure 1D**). Across all positions, mice showed a significant difference ( $12.1 \pm 3.2$  % mean  $\pm$  SD;  $p = 2.6\text{e-}4$ , *t*-test) in lick left probability for  $15^\circ$  angle differences (**Figure 1E**). This shows that head-fixed mice can discriminate object angle with a single whisker to at least  $15^\circ$  of precision.

#### *Sensorimotor features that discriminate object angle and drive choice*

To determine the sensorimotor features of touch that could be used to discriminate object angle, we recorded whisker motion and pole interaction from two perspectives at 310 fps during active object exploration (**Figures 2A and S3A-D**). We traced both views of the whisker automatically (Janelia Whisker Tracker) and generated a frame-by-frame three dimensional reconstruction of the whisker (26,807,476 frames; out of 26,878,629 recorded frames, 18,004 trials, 36 sessions, 12 mice, 3D reconstruction error rate  $0.998 \pm 4.35\text{e-}6$  frames per trial) with semi-automated contact detection (**Figures 2A, and S3C-D; Methods**).

We quantified twelve sensorimotor features associated with whisker-object interactions (**Methods**). These included six features of whisker kinematics (*i.e.* whisker motion) at touch onset: azimuthal angle at follicle ( $\theta$ ), elevation angle at follicle ( $\phi$ ), horizontal curvature ( $\kappa_H$ ), vertical curvature ( $\kappa_V$ ), length along the whisker from the base to contact point (arc length), and number of touches in a trial (touch count). These also included six features of whisker dynamics during touch (*i.e.* force generating features): maximum change in azimuthal angle ( $\text{max}\Delta\theta$ ), maximum change in elevation angle (vertical displacement;  $\text{max}\Delta\phi$ ), maximum change in horizontal curvature ( $\text{max}\Delta\kappa_H$ ), maximum change in vertical curvature (vertical bending;  $\text{max}\Delta\kappa_V$ ), distance slid along the object during a protracting whisk (slide distance), and time spent touching object during a protracting whisk (touch duration) (**Figures 2A-C**). Features were selected based on previous studies about those encoded in S1 ( $\theta$  (Ranganathan et al., 2018),  $\Delta\kappa_H$  (Peron et al., 2015)) and their vertical counterparts ( $\phi$ ,  $\Delta\kappa_V$ ), their kinematic and dynamic

counterparts ( $\Delta\theta$ ,  $\kappa_H$ ,  $\Delta\phi$ ,  $\kappa_V$ ), and those encoded in trigeminal ganglion (touch count, touch duration (Szwed et al., 2003) and its spatial counterpart, slide distance; arc length (Szwed et al., 2006)).

Most of these sensorimotor features had highly overlapping distributions between 45° and 135° pole presentations (**Figures 2D, and S4A, left**), with two notable exceptions, vertical bending ( $\max\Delta\kappa_V$ ) and vertical displacement ( $\max\Delta\phi$ ). The distributions of these two features were distinct and predominantly opposite sign between the two angles. This distinction was present in both naive and expert sessions (**Figure 2E, left**). A binomial generalized linear model (GLM) with lasso regularization using all 12 features ('full model') classified object angle with high accuracy (Matthew's correlation coefficient (MCC)  $0.930 \pm 0.049$  naive,  $0.961 \pm 0.015$  expert; **Figures 2F and S4B, left, Methods**). Single feature binomial GLMs classified angle poorly, except for those using  $\max\Delta\phi$  or  $\max\Delta\kappa_V$  (MCC  $0.796 \pm 0.047$  and  $0.886 \pm 0.037$ , respectively, in naive;  $0.794 \pm 0.069$  and  $0.8715 \pm 0.134$ , in expert; **Figure S4B, left**). Testing with 'leave-one-out' multinomial GLMs (Fisher et al., 2019; **Methods**) revealed that  $\max\Delta\kappa_V$  and  $\max\Delta\phi$  had higher variable importance than all other features (**Figures 2G and S4C, left**). Thus, we conclude that vertical bending and vertical displacement of the whisker during touch are the most informative sensorimotor features for coarse (2-angle) object-angle discrimination.

We applied a similar approach to determine which sensorimotor features mice *actually used* to discriminate object angle. When segregated by mouse choice (*i.e.* lick left or right) rather than object angle, the distributions of all sensorimotor features were indistinguishable in naive sessions, as expected from random guessing (**Figures 2E, right top, and S4A, right top**). Choice could not be classified by single or all features (**Figures 2F, S4B, right top**). In contrast, the distributions of features on expert sessions were highly similar to those segregated by object angle (**Figures 2E, bottom, and S4A, bottom**). This similarity reflects the high performance of mice on the task. Again, vertical bending ( $\max\Delta\kappa_V$ ) and vertical displacement ( $\max\Delta\phi$ ) had the most distinct distributions. Binomial GLM classifiers based on single features showed that  $\max\Delta\kappa_V$  and  $\max\Delta\phi$  performed comparably well in predicting choice in expert sessions (MCC  $0.717 \pm 0.028$ ,  $0.592 \pm 0.065$ ,  $\max\Delta\kappa_V$  and  $\max\Delta\phi$ , respectively;  $p = 0.0707$ , *t*-test; **Figure S4B, right bottom**). Contrary to the angle classifier, testing with a 'leave-one-out' choice

classifier revealed that the variable importance of  $\max\Delta\kappa_V$  dominates  $\max\Delta\phi$  and all other features (**Figures 2H and S4C, right bottom**). This was confirmed by comparing absolute coefficient values (**Figure S4D**). These results suggest that the predictive power of vertical displacement is primarily due to its correlation with vertical bending. Thus, we conclude that the degree of vertical bending of the whisker during touch is the primary feature that mice use to discriminate object angle and choose to lick left or right in 2-angle discrimination.

While a single sensorimotor feature was sufficient to discriminate two well-separated angles, finer discrimination may require more than one sensorimotor feature. In naive 7-angle sessions (**Figure 3A**), distributions of  $\max\Delta\kappa_V$ ,  $\max\Delta\phi$ , and slide distance showed strong relationships with object angle (**Figures 3B and S5A**), which led to higher than average multinomial GLM angle classification performance for each (**Figures 3C and S5B**). However, no single feature GLM came close to the full model (12-feature multinomial GLM) in 7-angle classification performance (**Figures 3C-D and S5B**). The ‘leave-one-out’ method showed that slide distance and  $\max\Delta\kappa_V$  were the most important whisker features, while  $\max\Delta\phi$  became negligible (**Figures 3E and S5C**). Coefficient values were in accordance with variable importance (**Figures S5D-E**). The simplest interpretation of this is that the high correlation of  $\max\Delta\kappa_V$  and  $\max\Delta\phi$  provided redundant information for fine angle discrimination, while slide distance provided complementary information (**Figure 3F**).

Despite the utility of slide distance in angle classification in both naive and expert 7-angle sessions (**Figures S6A-C**), it showed little predictive power in a binomial GLM *choice* classifier in expert 7-angle sessions (**Figures S6D-E**). Moreover,  $\max\Delta\kappa_V$  remained the dominant feature in multinomial GLM choice classification (**Figure S6F**). Thus, although slide distance was highly informative for discriminating fine angles, it did not drive choice, likely because the choice was binary. These results identified the primary tactile features that discriminate object angle and drive perception, which suggests they must also influence corresponding neural representations.

### *Neural representations of object angle in primary somatosensory cortex*

To investigate the neural basis of tactile object-angle perception, we performed 2-photon volumetric calcium imaging with GCaMP6s in excitatory neurons of L2 to L4 of barrel cortex during 7-angle discrimination ( $n = 12$  mice; TRE-GCaMP6s X CaMKII $\alpha$ -tTA; **Methods**). Data processing and region-of-interest detection was done using suite2p (Pachitariu et al., 2017) with manual curation, and spike inference was done using MLspike (Deneux et al., 2016). Active neurons were defined by their calcium traces (**Methods**). We first focused on naive sessions. On average, in naive mice ( $n = 12$ ), we imaged  $444 \pm 49$  active neurons in L2/3 C2,  $821 \pm 75$  in L2/3 non-C2,  $136 \pm 32$  in L4 C2, and  $182 \pm 38$  in L4 non-C2 per mouse.

To identify touch-responsive neurons, we built an ‘object model’ Poisson GLM with lasso regularization for each neuron that fit observed spike trains (inferred from calcium trace deconvolution) using five event classes (*i.e.* touch, whisking, licking, sound, and reward; **Figure 4A; Methods**). The lasso regularization enabled us to separate the effects of events other than touch on inferred spikes that happened in the same time bin as touch. Among active neurons,  $36.8 \pm 3.3$  % had inferred spikes fit by the GLM, defined as a goodness-of-fit  $> 0.1$  (**Figure 4B; Methods**). Each fit neuron was assigned zero, one, or more classes based on a ‘leave-one-out’ approach. Exclusively touch was by far the most common among fit neurons. Of all active neurons,  $23.5 \pm 2.8$  % were responsive to touch. Whisking and mixed touch & whisking made up most of the rest of the fit neurons, with  $< 1$  % of fit neurons assigned to licking, sound, or reward (**Figure 4C**).

We next tested the extent to which touch-responsive neurons encoded the angle of touched objects. Angle tuning was determined by one-way analysis of variance (ANOVA) of responses across angles, and subsequently confirmed by a shuffling test to minimize false-positives (**Figure 4D; Methods**). To prevent potential signal contamination from behavioral outcome, calculations were restricted to touch frames before the answer lick. Among touch-responsive neurons,  $78.0 \pm 2.3$  % were tuned to specific object angles in 12 naive mice.

Touch response patterns were diverse. They could be grouped into four categories: specific-tuned, where the maximum response was significantly different from all the other responses (**Figure 4D, i**), broad-tuned, where two or more responses from adjacent angles were

similar between themselves but significantly different from the rest (**Figure 4D, ii**), complex-tuned, where two or more responses from non-adjacent angles were similar between themselves but significantly different from the rest (**Figure 4D, iii**), and non-selective, where no response was significantly different from another (**Figure 4D, iv**). The ratio between the three tuned groups was roughly 3:5:2 (**Figure 4E, pie chart**). Tuned responses were found across all layers, including L4, which we confirmed in a pair of Scnn1a-Tg3-Cre mice that exclusively expressed GCaMP6s in L4 (LeMessurier et al., 2019; Madisen et al., 2015) (**Methods, Figure S7**). We characterized angle discriminability using two metrics: modulation (maximum response – minimum response) and sharpness (maximum response – mean response of the rest). Sharpness was highest in specific-tuned neurons, while modulation was similar between specific-tuned and broad-tuned neurons (**Figure 4E**). Complex-tuned neurons had less modulation and sharpness, implying weaker angle discriminability (**Figure 4E**). Maximally-preferred angles tiled the tested space (**Figure 4F**). However, the distribution was not uniform; over half of the neurons were tuned to extreme angles, 45° and 135° (**Figure 4G**).

#### *Sensorimotor features that drive object-angle tuning*

We next sought to understand the sensorimotor basis of object-angle tuning in S1. That is, what whisker kinematic and dynamic features establish angle-specific neural responses? To identify these features, we built a ‘sensorimotor model’ for each touch-responsive neuron (**Figure 5A**) by swapping the touch input parameters of the ‘object model’ (**Figure 4A**) with the 12 whisker features we previously used to predict object angle (**Figure 2**). Goodness-of-fit values for neurons using this ‘sensorimotor model’ were highly correlated to the ‘object model’ ( $R^2 = 0.795$ ; **Figure S8A**). Only  $4.2 \pm 0.47\%$  of neurons fit by the ‘object model’ failed to meet fit criteria of the ‘sensorimotor model’. The absolute difference between goodness-of-fit for whisker vs. object models was  $< 0.1$  for  $> 95\%$  of fit neurons (**Figure S8B**). Out of all angle-tuned neurons,  $87.53 \pm 2.54\%$  were also angle-tuned in the sensorimotor model, and further analysis was restricted to these neurons. The sensorimotor model spike output recapitulated the observed object-angle tuning, albeit with somewhat more neurons preferring extreme angles (**Figure S8C**). Less than 15 % of tuned neurons shifted their angle preference by more

than 15° when using the ‘sensorimotor model’. Thus, the sensorimotor features of whisker touch used in this model were sufficient to accurately represent angle-tuned responses of neurons.

We identified four features that could *potentially* influence angle tuning by comparing variable importance between angle-tuned and non-selective touch neurons. Vertical bending ( $\max\Delta\kappa_v$ ), slide distance, vertical displacement ( $\max\Delta\phi$ ), and vertical curvature at touch onset ( $\kappa_v$ ) had higher variable importance and were more frequently fit in angle-tuned neurons compared to non-selective neurons (**Figures 5B and S8D-F**).

To quantify the impact of each feature on angle tuning, we calculated the correlation between observed angle-tuning curves of inferred spikes and ‘leave-one-out’ reconstructions from the sensorimotor model, for each neuron (**Figure 5C**). For example, if  $\max\Delta\kappa_v$  impacted the angle tuning more compared to other whisker features, removing this parameter from the full ‘sensorimotor model’ would reduce the correlation between tuning curves more than removing other features (**Figure 5C, top**). The most impactful sensorimotor feature for each neuron was diverse and spatially distributed (**Figure 5D**). The average correlation between ‘sensorimotor model’ and inferred spikes was  $0.828 \pm 0.015$  (**Figure S8G**), which provided the upper limit value of the impact on tuning curve. Removing the most important single feature in each neuron reduced correlation by  $0.318 \pm 0.020$ , showing that most angle tuning reflects more than one whisker feature, and providing the upper limit of single feature impact (max feature in **Figure 5E**).

Vertical bending ( $\max\Delta\kappa_v$ ) and slide distance were the most important features in predicting angle tuning across the population, with each having a similar impact to the other 10 features combined (**Figures 5E-F**). This corroborates their increased variable importance in angle-tuned neurons (**Figure 5B**). These two features had much greater impact on tuning curve shape and angle preference than any other feature (**Figures S8H-I**). This remained true in expert sessions (**Figure S8J**). The impact of removing these two features was additive, suggesting they make independent contributions to the population distribution of angle tuning (**Figures 5E-F**). Moreover, these were also the two most informative features for fine discrimination of object

angle (**Figures 3E, S5C,E, and S6C,E**), showing that angle-specific tuning of S1 neurons is established by the most angle-discriminative sensorimotor features at the sensory periphery.

#### *Stable object-angle tuning after learning despite active ensemble turnover*

To what extent do sensorimotor representations in primary sensory cortex change during associative learning of stimulus with reward? To answer this question, we tracked active neurons in matched 7-angle sessions before and after learning (11,351 neurons from 12 matched sessions in 6 mice, **Methods**, **Figure 6A**), which were separated by an average of  $16 \pm 2$  sessions. Remarkably, only  $39.1 \pm 3.8\%$  of tracked neurons were active in both sessions (*i.e.* persistent neurons), with more superficial imaging planes showing higher turnover (**Figure 6B**). About half of the neurons active during naive sessions fell silent after training, regardless of category (*i.e.* non-touch, non-selective touch, angle-tuned touch) (**Figures 6C, D**). Similarly, about half of the neurons active during expert sessions had previously been silent, regardless of category (**Figures 6C,E**).

The overall numbers of newly recruited and eliminated neurons (*i.e.* transient neurons) were not perfectly balanced (**Figure 6C**), with significantly fewer active neurons in expert sessions ( $88.3 \pm 3.9\%$ ,  $n = 6$ ,  $p = 0.0297$ , paired *t*-test). However, the average spike rate of neurons was higher in expert sessions ( $0.404 \pm 0.018$  vs  $0.472 \pm 0.037$ , naive and expert, respectively;  $p = 0.0500$ , paired *t*-test), resulting in a homeostasis of population activity (summed population spike rate in expert / in naive sessions,  $1.031 \pm 0.080$ ,  $p = 0.716$ ,  $n = 6$ , *t*-test to 1; **Figure 6F**). On average, transient neurons had lower spike rates compared to persistent neurons, regardless of learning (**Figure 6G**).

Despite the dramatic changes in active ensemble membership, the overall distribution of angle preference was nearly identical between naive and expert sessions (**Figure 7A**), with no change in the relative representation of  $45^\circ$  and  $135^\circ$  angle preferring neurons (which were the object angles used during training). Expert sessions showed small, but non-significant increases in preferred angle response magnitude (**Figure 7B**), tuning modulation depth (**Figure 7C**), and tuning sharpness (**Figure 7D**). Thus, the overall representation of object angles remained stable despite high turnover of active ensemble membership.

A closer look into the reorganization of activity across training revealed that persistent angle-tuned neurons (angle-tuned → angle-tuned) were remarkably stable in all angle-tuning characteristics. Their mean firing rate (**Figure 8A**), touch-evoked response size (**Figure 8B**), tuning modulation (**Figure 8C**), sharpness (**Figure 8D**), and population distribution of angle preference (**Figure 8E**) was unchanged with training. Moreover, matched neurons before and after training showed remarkable stability of angle preference (**Figure 8F**). On the other hand, transient angle-tuned neurons (silent → angle-tuned, or angle-tuned → silent) showed important differences in some angle-tuning characteristics. Similar to persistent angle-tuned neurons before and after training, the population distribution of angle preference between recruited and eliminated angle-tuned neurons was indistinguishable (**Figures 8G-H**). However, recruited angle-tuned neurons had deeper and sharper angle-tuning (**Figures 8C-D**). This suggests that for each angle representation in S1, there is a core group of highly selective neurons that maintains a stable representation of it across training, with less selective neurons eliminated from the representation in favor of more selective neurons.

## Discussion

We demonstrated that head-fixed mice can discriminate object angle to at least 15° resolution using a single whisker (**Figure 1**). We identified two sensorimotor features (vertical bending and vertical displacement) that discriminate object angle (2-angle task), and showed that only vertical bending is used by expert mice to make coarse angle discriminations (**Figure 2**). An additional feature, slide distance, was required for fine angle discrimination (7-angle task; **Figure 3**). We mapped the neural representation of object angle across layers of S1 and found distinct sets of neurons tuned for each presented angle, with the extreme angles (45° and 135°) overrepresented in the tuned population (**Figure 4**). The two sensorimotor features most important for fine angle discrimination (vertical bending and slide distance) also had the largest influence on the angle-tuning curve of neural responses (**Figure 5**). Training resulted in high turnover in active ensemble membership (**Figure 6**). Despite this, the relative proportion of neurons tuned to each angle was stable across learning (**Figure 7**). However, training increased the depth and sharpness of angle-tuning by replacement of more weakly tuned neurons with more strongly tuned ones. (**Figure 8**).

We note several limitations of our work. We only used the 12 sensorimotor features we thought most likely to vary with object angle or influence S1 activity. This likely fails to completely capture whisker mechanics (Huet et al., 2015; Isett et al., 2018) that drive primary afferents (Severson et al., 2017; Wallach et al., 2016). However, using only linear models, this set of features was able to discriminate 2-angles at >95% accuracy (**Figure 2F**) and beat expert mice in virtual psychometric performance on 7-angle discrimination (**Figure S7G-H**). Thus, while not comprehensive, these features provided sufficient information to accurately identify the sensorimotor drivers of behavior and neural activity in tactile object-angle discrimination.

We did not present angles beyond 45 and 135 degrees for two reasons. First, shallow object angles (< 45° or > 135°) are less likely to be touched, because mice mostly whisk back and forth within a near-horizontal plane. Second, when touch does occur at shallow angles, the bias in azimuthal angle at touch onset is too large to overcome with a practical amount of

anteroposterior jitter. This could have permitted mice to use positional cues, rather than angle *per se*, to discriminate shallow angles.

It is unlikely that mice discriminated angle by integrating positional information across multiple touches, as performance greatly exceeded chance in trials with one pre-lick touch in 2-angle and radial jittered expert sessions (71% and 82% correct, respectively; **Figures S9A-B**). Moreover, on trials with multiple touches, there was no consistent relationship between the performance and the spatial spread of touch points (**Figures S9C-E**).

We also note several advantages over prior work. Our use of symmetric response (lick left/right; Peron et al., 2015) rather than go/no-go (Chen et al., 2015; Khan et al., 2018; Poort et al., 2015), spike deconvolution, and GLM based event assignments reduced potential confounding from neural signals of reward expectation and motor movements. We deployed a novel dual-view 3D whisker tracking and touch detection method (**Figure S3**) and rotatable pole to investigate a much wider range of tactile features (12 total, including vertical bending, vertical displacement and slide distance) than prior maps of S1 (Chen et al., 2015; Peron et al., 2015). This approach revealed that vertical forces and slide distance are powerful drivers of S1 and have a greater contribution to object-angle discrimination (**Figure 3**) and neural tuning (**Figure 5**) than horizontal forces.

Why is slide distance so important for driving neural responses? One possibility is that it captures mechanical features beyond the abilities of our imaging technology to detect and quantify (*e.g.* micro stick or slip events and vibrations faster than our camera frame rate). Many sensory afferents respond strongly to varying force or stresses related to stick and slip (Wolfe et al., 2008; Severson et al., 2017). Sensory variation during sliding along the pole, rather than sticking in one spot, could drive more sustained spiking in both sensory afferents and S1 (Chen et al., 2015; Isett et al., 2018; Jadhav et al., 2009). Sliding up or down a vertical pole is difficult to quantify from a single overhead view (Huet et al., 2015; Petersen et al., 2019), which could also contribute to variability in touch responses in prior work.

Why were the extreme angles 45° and 135° overrepresented in the S1 population tuning? The distribution of angle preference was unaffected by training, so the overrepresentation of extreme angles does not reflect an enhancement toward reward

predictive stimuli. It is possible that all angles 0-180° are equally represented, with neurons with preferences beyond 45° and 135° pooled into the two most extreme bins. An alternative explanation is that 45° and 135° angles produce a particularly strong combination of vertical bending, horizontal bending, and slide distance, and these features are the strongest dynamic drivers of S1 responses (**Figures S8D-F**). A third possibility is that deflections out of the plane of whisking and body movement could be more likely to represent behaviorally-relevant objects. Overrepresentation to cardinal directions is seen in primary visual cortex of carnivores (Bonds, 1982), which is ascribed to the impact of sensory experience (Blakemore and Cooper, 1970; Hirsch and Spinelli, 1970) and the statistics of natural stimuli (Girshick et al., 2011; Tomassini et al., 2010). An analogous explanation may apply to object-angle tuning in S1.

The dominant reorganization across learning was recruitment into or elimination from the active ensemble (**Figures 6A-E**). The shift in active ensemble membership (**Figures 6D-E**) could reflect changing intrinsic excitability of excitatory neurons (Barth et al., 2004; Desai et al., 1999; Yiu et al., 2014) or of local inhibitory networks that enforce firing rate homeostasis (Dehorter et al., 2015; Gainey et al., 2018; Goldberg et al., 2008; **Figure 6F**). Neurons with greater intrinsic excitability, extrinsic drive (Jones, 2000), or recurrent connectivity (Cossell et al., 2015) would be more likely to remain active across sessions and learning. This is consistent with our finding that persistent neurons have significantly higher firing rates than transient neurons (**Figure 6G**).

How is representational stability maintained in the face of high active ensemble turnover? The simplest explanation is that neurons in S1 maintain stable stimulus selectivity across learning, independent of active ensemble participation. This would be consistent with results showing V1 neurons maintain stimulus selectivity before and after monocular deprivation (Rose et al., 2016) and CA1 neurons maintain place preference across weeks despite variation in active ensemble participation (Ziv et al., 2013). This possibility is supported by the remarkable stability of angle preference in persistent angle-tuned neurons (**Figure 8F**).

Our results potentially reconcile a debate over whether or not primary sensory cortical representations sharpen with training. Cross-sectional electrophysiological studies in primate primary visual cortex (V1) showed that, at a population level, the distribution of maximally

preferred orientation angle remained stable after grating orientation angle perceptual learning with (Schoups et al., 2001) or without (Ghose et al., 2002) sharpening around the trained orientation angle. Our longitudinal approach allows observation of the same cells across training, including active ensemble turnover. Sharpening of tuning was not significant in the whole population (**Figure 7**), but was significant within the subset of neurons that were transient members of the active ensemble (**Figure 8**). Thus, differences in sampling frequency between persistent and transient ensemble members could lead to opposing conclusions.

Overall, our data identify behavioral and neural bases of tactile angle discrimination, and how tactile representations evolve across learning. Our results support a model of learning where changes in active ensemble membership increase representational efficiency in S1, while persistent angle-tuned neurons provide a foundation of stable sensory representations upon which stable sensory percepts can be built.

## STAR★Methods

Detailed methods are provided in the supplementary text.

## References

- Adrian, E.D., and Zotterman, Y. (1926). The impulses produced by sensory nerve endings: Part 3. Impulses set up by Touch and Pressure. *J. Physiol.* **61**, 465–483.
- Arabzadeh, E., Zorzin, E., and Diamond, M.E. (2005). Neuronal Encoding of Texture in the Whisker Sensory Pathway. *PLOS Biol.* **3**, e17.
- Aronoff, R., Matyas, F., Mateo, C., Ciron, C., Schneider, B., and Petersen, C.C.H. (2010). Long-range connectivity of mouse primary somatosensory barrel cortex: Long-range connectivity of barrel cortex. *Eur. J. Neurosci.* **31**, 2221–2233.
- Bagdasarian, K., Szwed, M., Knutsen, P.M., Deutsch, D., Derdikman, D., Pietr, M., Simony, E., and Ahissar, E. (2013). Pre-neuronal morphological processing of object location by individual whiskers. *Nat. Neurosci.* **16**, 622–631.
- Bale, M.R., Davies, K., Freeman, O.J., Ince, R.A.A., and Petersen, R.S. (2013). Low-Dimensional Sensory Feature Representation by Trigeminal Primary Afferents. *J. Neurosci.* **33**, 12003–12012.
- Barth, A.L., Gerkin, R.C., and Dean, K.L. (2004). Alteration of Neuronal Firing Properties after In Vivo Experience in a FosGFP Transgenic Mouse. *J. Neurosci.* **24**, 6466–6475.
- Bensmaia, S.J., Denchev, P.V., Dammann, J.F., Craig, J.C., and Hsiao, S.S. (2008). The Representation of Stimulus Orientation in the Early Stages of Somatosensory Processing. *J. Neurosci.* **28**, 776–786.
- Blakemore, C., and Cooper, G.F. (1970). Development of the Brain depends on the Visual Environment. *Nature* **228**, 477–478.
- Bonds, A.B. (1982). An “oblique effect” in the visual evoked potential of the cat. *Exp. Brain Res.* **46**, 151–154.
- Bush, N.E., Schroeder, C.L., Hobbs, J.A., Yang, A.E., Huet, L.A., Solla, S.A., and Hartmann, M.J. (2016). Decoupling kinematics and mechanics reveals coding properties of trigeminal ganglion neurons in the rat vibrissal system. *ELife* **5**, e13969.
- Calford, M.B. (2002). Dynamic representational plasticity in sensory cortex. *Neuroscience* **111**, 709–738.
- Campagner, D., Evans, M.H., Bale, M.R., Erskine, A., and Petersen, R.S. (2016). Prediction of primary somatosensory neuron activity during active tactile exploration. *ELife* **18**.
- Carvell, G.E., and Simons, D.J. (1990). Biometric analyses of vibrissal tactile discrimination in the rat. *J. Neurosci.* **10**, 2638–2648.
- Caulier, L. (1995). Layer I of primary sensory neocortex: where top-down converges upon bottom-up. *Behav. Brain Res.* **71**, 163–170.
- Chen, J.L., Margolis, D.J., Stankov, A., Sumanovski, L.T., Schneider, B.L., and Helmchen, F. (2015). Pathway-specific reorganization of projection neurons in somatosensory cortex during learning. *Nat. Neurosci.* **18**, 1101–1108.
- Chen, T.-W., Wardill, T.J., Sun, Y., Pulver, S.R., Renninger, S.L., Baohan, A., Schreiter, E.R., Kerr, R.A., Orger, M.B., Jayaraman, V., et al. (2013). Ultrasensitive fluorescent proteins for imaging neuronal activity. *Nature* **499**, 295–300.
- Cheung, J., Maire, P., Kim, J., Sy, J., and Hires, S.A. (2019). The Sensorimotor Basis of Whisker-Guided Anteroposterior Object Localization in Head-Fixed Mice. *Curr. Biol.* **29**, 3029–3040.e4.

- Clack, N.G., O'Connor, D.H., Huber, D., Petreanu, L., Hires, A., Peron, S., Svoboda, K., and Myers, E.W. (2012). Automated Tracking of Whiskers in Videos of Head Fixed Rodents. *PLoS Comput. Biol.* **8**, e1002591.
- Clopath, C., Bonhoeffer, T., Hübener, M., and Rose, T. (2017). Variance and invariance of neuronal long-term representations. *Philos. Trans. R. Soc. B Biol. Sci.* **372**, 20160161.
- Cossell, L., Iacaruso, M.F., Muir, D.R., Houlton, R., Sader, E.N., Ko, H., Hofer, S.B., and Mrsic-Flogel, T.D. (2015). Functional organization of excitatory synaptic strength in primary visual cortex. *Nature* **518**, 399–403.
- Coste, B., Xiao, B., Santos, J.S., Syeda, R., Grandl, J., Spencer, K.S., Kim, S.E., Schmidt, M., Mathur, J., Dubin, A.E., et al. (2012). Piezo proteins are pore-forming subunits of mechanically activated channels. *Nature* **483**, 176–181.
- Dehorter, N., Ciceri, G., Bartolini, G., Lim, L., Pino, I. del, and Marín, O. (2015). Tuning of fast-spiking interneuron properties by an activity-dependent transcriptional switch. *Science* **349**, 1216–1220.
- Deneux, T., Kaszas, A., Szalay, G., Katona, G., Lakner, T., Grinvald, A., Rózsa, B., and Vanzetta, I. (2016). Accurate spike estimation from noisy calcium signals for ultrafast three-dimensional imaging of large neuronal populations *in vivo*. *Nat. Commun.* **7**, 1–17.
- Desai, N.S., Rutherford, L.C., and Turrigiano, G.G. (1999). Plasticity in the intrinsic excitability of cortical pyramidal neurons. *Nat. Neurosci.* **2**, 515–520.
- Druckmann, S., and Chklovskii, D.B. (2012). Neuronal Circuits Underlying Persistent Representations Despite Time Varying Activity. *Curr. Biol.* **22**, 2095–2103.
- Fisher, A., Rudin, C., and Dominici, F. (2019). All Models are Wrong, but Many are Useful: Learning a Variable's Importance by Studying an Entire Class of Prediction Models Simultaneously. *ArXiv180101489 Stat.*
- Fitzgerald, P.J., Lane, J.W., Thakur, P.H., and Hsiao, S.S. (2004). Receptive Field Properties of the Macaque Second Somatosensory Cortex: Evidence for Multiple Functional Representations. *J. Neurosci.* **24**, 11193–11204.
- Gainey, M.A., Aman, J.W., and Feldman, D.E. (2018). Rapid Disinhibition by Adjustment of PV Intrinsic Excitability during Whisker Map Plasticity in Mouse S1. *J. Neurosci.* **38**, 4749–4761.
- Gardner, E.P., and Palmer, C.I. (1989). Simulation of motion on the skin. I. Receptive fields and temporal frequency coding by cutaneous mechanoreceptors of OPTACON pulses delivered to the hand. *J. Neurophysiol.* **62**, 1410–1436.
- Ghose, G.M., Yang, T., and Maunsell, J.H.R. (2002). Physiological Correlates of Perceptual Learning in Monkey V1 and V2. *J. Neurophysiol.* **87**, 1867–1888.
- Gibson, E.J. (1963). Perceptual Learning. *Annu. Rev. Psychol.* **14**, 29–56.
- Gibson, J.J. (1962). Observations on active touch. *Psychol. Rev.* **69**, 477–491.
- Gilbert, C.D., and Li, W. (2013). Top-down influences on visual processing. *Nat. Rev. Neurosci.* **14**, 350–363.
- Girshick, A.R., Landy, M.S., and Simoncelli, E.P. (2011). Cardinal rules: visual orientation perception reflects knowledge of environmental statistics. *Nat. Neurosci.* **14**, 926–932.
- Goldberg, E.M., Clark, B.D., Zagha, E., Nahmani, M., Erisir, A., and Rudy, B. (2008). K<sup>+</sup> Channels at the Axon Initial Segment Dampen Near-Threshold Excitability of Neocortical Fast-Spiking GABAergic Interneurons. *Neuron* **58**, 387–400.
- Harvey, M.A., Bermejo, R., and Zeigler, H.P. (2001). Discriminative whisking in the head-fixed rat: optoelectronic monitoring during tactile detection and discrimination tasks. *Somatosens. Mot. Res.* **18**, 211–222.
- von Heimendahl, M., Itskov, P.M., Arabzadeh, E., and Diamond, M.E. (2007). Neuronal Activity in Rat Barrel Cortex Underlying Texture Discrimination. *PLOS Biol.* **5**, e305.

- Hensel, H., and Boman, K.K.A. (1960). Afferent impulses in cutaneous sensory nerves in human subjects. *J. Neurophysiol.* 23, 564–578.
- Hires, S.A., Gutnisky, D.A., Yu, J., O'Connor, D.H., and Svoboda, K. (2015). Low-noise encoding of active touch by layer 4 in the somatosensory cortex. *ELife* 4, e06619.
- Hirsch, H.V.B., and Spinelli, D.N. (1970). Visual Experience Modifies Distribution of Horizontally and Vertically Oriented Receptive Fields in Cats. *Science* 168, 869–871.
- Holtmaat, A., and Svoboda, K. (2009). Experience-dependent structural synaptic plasticity in the mammalian brain. *Nat. Rev. Neurosci.* 10, 647–658.
- Horikawa, K., Yamada, Y., Matsuda, T., Kobayashi, K., Hashimoto, M., Matsu-ura, T., Miyawaki, A., Michikawa, T., Mikoshiba, K., and Nagai, T. (2010). Spontaneous network activity visualized by ultrasensitive Ca<sup>2+</sup> indicators, yellow Cameleon-Nano. *Nat. Methods* 7, 729–732.
- Huet, L.A., Schroeder, C.L., and Hartmann, M.J.Z. (2015). Tactile signals transmitted by the vibrissa during active whisking behavior. *J. Neurophysiol.* 113, 3511–3518.
- Iggo, A. (1962). An electrophysiological analysis of afferent fibres in primate skin. *Acta Neuroveg. (Wien)* 24, 225–240.
- Isett, B.R., Feasel, S.H., Lane, M.A., and Feldman, D.E. (2018). Slip-Based Coding of Local Shape and Texture in Mouse S1. *Neuron* 97, 418–433.e5.
- Jadhav, S.P., Wolfe, J., and Feldman, D.E. (2009). Sparse temporal coding of elementary tactile features during active whisker sensation. *Nat. Neurosci.* 12, 792–800.
- James, W. (1890). The principles of psychology, Vol II (NY, US: Henry Holt and Company).
- Jones, E.G. (2000). Cortical and Subcortical Contributions to Activity-Dependent Plasticity in Primate Somatosensory Cortex. *Annu. Rev. Neurosci.* 23, 1–37.
- Jurjut, O., Georgieva, P., Busse, L., and Katzner, S. (2017). Learning Enhances Sensory Processing in Mouse V1 before Improving Behavior. *J. Neurosci.* 37, 6460–6474.
- Katz, D. (1925). Der Autbau der Tastwelt. *Z. Für Psychol. Ergänzungsband* 11.
- Khan, A.G., Poort, J., Chadwick, A., Blot, A., Sahani, M., Mrsic-Flogel, T.D., and Hofer, S.B. (2018). Distinct learning-induced changes in stimulus selectivity and interactions of GABAergic interneuron classes in visual cortex. *Nat. Neurosci.* 21, 851–859.
- Lederman, S.J., and Klatzky, R.L. (1987). Hand movements: A window into haptic object recognition. *Cognit. Psychol.* 19, 342–368.
- LeMessurier, A.M., and Feldman, D.E. (2018). Plasticity of population coding in primary sensory cortex. *Curr. Opin. Neurobiol.* 53, 50–56.
- LeMessurier, A.M., Laboy-Juárez, K.J., McClain, K., Chen, S., Nguyen, T., and Feldman, D.E. (2019). Enrichment drives emergence of functional columns and improves sensory coding in the whisker map in L2/3 of mouse S1. *ELife* 8, e46321.
- Li, L., Rutlin, M., Abraira, V.E., Cassidy, C., Kus, L., Gong, S., Jankowski, M.P., Luo, W., Heintz, N., Koerber, H.R., et al. (2011). The Functional Organization of Cutaneous Low-Threshold Mechanosensory Neurons. *Cell* 147, 1615–1627.
- Luo, L., Callaway, E.M., and Svoboda, K. (2008). Genetic Dissection of Neural Circuits. *Neuron* 57, 634–660.
- Lütcke, H., Margolis, D.J., and Helmchen, F. (2013). Steady or changing? Long-term monitoring of neuronal population activity. *Trends Neurosci.* 36, 375–384.

Madisen, L., Garner, A.R., Shimaoka, D., Chuong, A.S., Klapoetke, N.C., Li, L., van der Bourg, A., Niino, Y., Egolf, L., Monetti, C., et al. (2015). Transgenic Mice for Intersectional Targeting of Neural Sensors and Effectors with High Specificity and Performance. *Neuron* *85*, 942–958.

Makino, H., and Komiyama, T. (2015). Learning enhances the relative impact of top-down processing in the visual cortex. *Nat. Neurosci.* *18*, 1116–1122.

Manita, S., Suzuki, T., Homma, C., Matsumoto, T., Odagawa, M., Yamada, K., Ota, K., Matsubara, C., Inutsuka, A., Sato, M., et al. (2015). A Top-Down Cortical Circuit for Accurate Sensory Perception. *Neuron* *86*, 1304–1316.

Margolis, D.J., Lütcke, H., Schulz, K., Haiss, F., Weber, B., Kügler, S., Hasan, M.T., and Helmchen, F. (2012). Reorganization of cortical population activity imaged throughout long-term sensory deprivation. *Nat. Neurosci.* *15*, 1539–1546.

McCarter, G.C., Reichling, D.B., and Levine, J.D. (1999). Mechanical transduction by rat dorsal root ganglion neurons in vitro. *Neurosci. Lett.* *273*, 179–182.

Mehta, S.B., Whitmer, D., Figueroa, R., Williams, B.A., and Kleinfeld, D. (2007). Active Spatial Perception in the Vibrissa Scanning Sensorimotor System. *PLOS Biol.* *5*, e15.

O'Connor, D.H., Clack, N.G., Huber, D., Komiyama, T., Myers, E.W., and Svoboda, K. (2010). Vibrissa-Based Object Localization in Head-Fixed Mice. *J. Neurosci.* *30*, 1947–1967.

Pachitariu, M., Stringer, C., Dipoppa, M., Schröder, S., Rossi, L.F., Dalgleish, H., Carandini, M., and Harris, K.D. (2017). Suite2p: beyond 10,000 neurons with standard two-photon microscopy. *BioRxiv* 061507.

Pammer, L., O'Connor, D.H., Hires, S.A., Clack, N.G., Huber, D., Myers, E.W., and Svoboda, K. (2013). The Mechanical Variables Underlying Object Localization along the Axis of the Whisker. *J. Neurosci.* *33*, 6726–6741.

Peron, S.P., Freeman, J., Iyer, V., Guo, C., and Svoboda, K. (2015). A Cellular Resolution Map of Barrel Cortex Activity during Tactile Behavior. *Neuron* *86*, 783–799.

Petersen, R.S., Brambilla, M., Bale, M.R., Alenda, A., Panzeri, S., Montemurro, M.A., and Maravall, M. (2008). Diverse and Temporally Precise Kinetic Feature Selectivity in the VPm Thalamic Nucleus. *Neuron* *60*, 890–903.

Petersen, R.S., Rodriguez, A.C., Evans, M.H., Campagner, D., and Loft, M.S.E. (2019). A system for tracking whisker kinematics and whisker shape in three dimensions. *BioRxiv* 773697.

Phillips, J.R., and Johnson, K.O. (1981). Tactile spatial resolution. II. Neural representation of Bars, edges, and gratings in monkey primary afferents. *J. Neurophysiol.* *46*, 1192–1203.

Pluta, S.R., Lyall, E.H., Telian, G.I., Ryapolova-Webb, E., and Adesnik, H. (2017). Surround Integration Organizes a Spatial Map during Active Sensation. *Neuron* *94*, 1220–1233.e5.

Poort, J., Khan, A.G., Pachitariu, M., Nemri, A., Orsolic, I., Krupic, J., Bauza, M., Sahani, M., Keller, G.B., Mrsic-Flogel, T.D., et al. (2015). Learning Enhances Sensory and Multiple Non-sensory Representations in Primary Visual Cortex. *Neuron* *86*, 1478–1490.

Pruszynski, J.A., and Johansson, R.S. (2014). Edge-orientation processing in first-order tactile neurons. *Nat. Neurosci.* *17*, 1404–1409.

Pubols, L.M., and Leroy, R.F. (1977). Orientation detectors in the primary somatosensory neocortex of the raccoon. *Brain Res.* *129*, 61–74.

Ranganathan, G.N., Apostolides, P.F., Harnett, M.T., Xu, N.-L., Druckmann, S., and Magee, J.C. (2018). Active dendritic integration and mixed neocortical network representations during an adaptive sensing behavior. *Nat. Neurosci.* *21*, 1583–1590.

Roland, P.E., and Mortensen, E. (1987). Somatosensory detection of microgeometry, macrogeometry and kinesthesia in man. *Brain Res. Rev.* *12*, 1–42.

- Rose, T., Jaepel, J., Hubener, M., and Bonhoeffer, T. (2016). Cell-specific restoration of stimulus preference after monocular deprivation in the visual cortex. *Science* *352*, 1319–1322.
- Sakurai, K., Akiyama, M., Cai, B., Scott, A., Han, B.-X., Takatoh, J., Sigrist, M., Arber, S., and Wang, F. (2013). The Organization of Submodality-Specific Touch Afferent Inputs in the Vibrissa Column. *Cell Rep.* *5*, 87–98.
- Schoups, A., Vogels, R., Qian, N., and Orban, G. (2001). Practising orientation identification improves orientation coding in V1 neurons. *Nature* *412*, 549–553.
- Severson, K.S., Xu, D., Van de Loo, M., Bai, L., Ginty, D.D., and O'Connor, D.H. (2017). Active Touch and Self-Motion Encoding by Merkel Cell-Associated Afferents. *Neuron* *94*, 666–676.e9.
- Shipley, M.T. (1974). Response characteristics of single units in the rat's trigeminal nuclei to vibrissa displacements. *J. Neurophysiol.* *37*, 73–90.
- Sofroniew, N.J., Vlasov, Y.A., Hires, S.A., Freeman, J., and Svoboda, K. (2015). Neural coding in barrel cortex during whisker-guided locomotion. *ELife* *4*, e12559.
- Szwed, M., Bagdasarian, K., and Ahissar, E. (2003). Encoding of Vibrissal Active Touch. *Neuron* *40*, 621–630.
- Szwed, M., Bagdasarian, K., Blumenfeld, B., Barak, O., Derdikman, D., and Ahissar, E. (2006). Responses of Trigeminal Ganglion Neurons to the Radial Distance of Contact During Active Vibrissal Touch. *J. Neurophysiol.* *95*, 791–802.
- Tomassini, A., Morgan, M.J., and Solomon, J.A. (2010). Orientation uncertainty reduces perceived obliquity. *Vision Res.* *50*, 541–547.
- Usoskin, D., Furlan, A., Islam, S., Abdo, H., Lönnberg, P., Lou, D., Hjerling-Leffler, J., Haeggström, J., Kharchenko, O., Kharchenko, P.V., et al. (2015). Unbiased classification of sensory neuron types by large-scale single-cell RNA sequencing. *Nat. Neurosci.* *18*, 145–153.
- Vallbo, A.B., and Johansson, R.S. (1984). Properties of cutaneous mechanoreceptors in the human hand related to touch sensation. *Hum. Neurobiol.* *3*, 3–14.
- Vincent, S.B. (1912). The function of the vibrissae in the behavior of the white rat. *Behav Monogr.* *1*, 7–81.
- Wallach, A., Bagdasarian, K., and Ahissar, E. (2016). On-going computation of whisking phase by mechanoreceptors. *Nat. Neurosci.* *19*, 487–493.
- Weinberger, N.M. (1995). Dynamic Regulation of Receptive Fields and Maps in the Adult Sensory Cortex. *Annu. Rev. Neurosci.* *30*.
- Wekselblatt, J.B., Flister, E.D., Piscopo, D.M., and Niell, C.M. (2016). Large-scale imaging of cortical dynamics during sensory perception and behavior. *J. Neurophysiol.* *115*, 2852–2866.
- Welker, C. (1971). Microelectrode delineation of fine grain somatotopic organization of Sml cerebral neocortex in albino rat. *Brain Res.* *26*, 259–275.
- Werner, G., and Mountcastle, V.B. (1965). Neural activity in mechanoreceptive cutaneous afferents: stimulus-response relations, weber functions, and information transmission. *J. Neurophysiol.* *28*, 359–397.
- White, E.L., and DeAmicis, R.A. (1977). Afferent and efferent projections of the region in mouse sml cortex which contains the posteromedial barrel subfield. *J. Comp. Neurol.* *175*, 455–481.
- Woolsey, T.A., and Van der Loos, H. (1970). The structural organization of layer IV in the somatosensory region (S I) of mouse cerebral cortex: The description of a cortical field composed of discrete cytoarchitectonic units. *Brain Res.* *17*, 205–242.

Yiu, A.P., Mercaldo, V., Yan, C., Richards, B., Rashid, A.J., Hsiang, H.-L.L., Pressey, J., Mahadevan, V., Tran, M.M., Kushner, S.A., et al. (2014). Neurons Are Recruited to a Memory Trace Based on Relative Neuronal Excitability Immediately before Training. *Neuron* *83*, 722–735.

Zhang, S., Xu, M., Kamigaki, T., Do, J.P.H., Chang, W.-C., Jenvay, S., Miyamichi, K., Luo, L., and Dan, Y. (2014). Long-range and local circuits for top-down modulation of visual cortex processing. *Science* *345*, 660–665.

Ziv, Y., Burns, L.D., Cocker, E.D., Hamel, E.O., Ghosh, K.K., Kitch, L.J., Gamal, A.E., and Schnitzer, M.J. (2013). Long-term dynamics of CA1 hippocampal place codes. *Nat. Neurosci.* *16*, 264–266.

Zucker, E., and Welker, W.I. (1969). Coding of somatic sensory input by vibrissae neurons in the rat's trigeminal ganglion. *Brain Res.* *12*, 138–156.

**Figure 1**

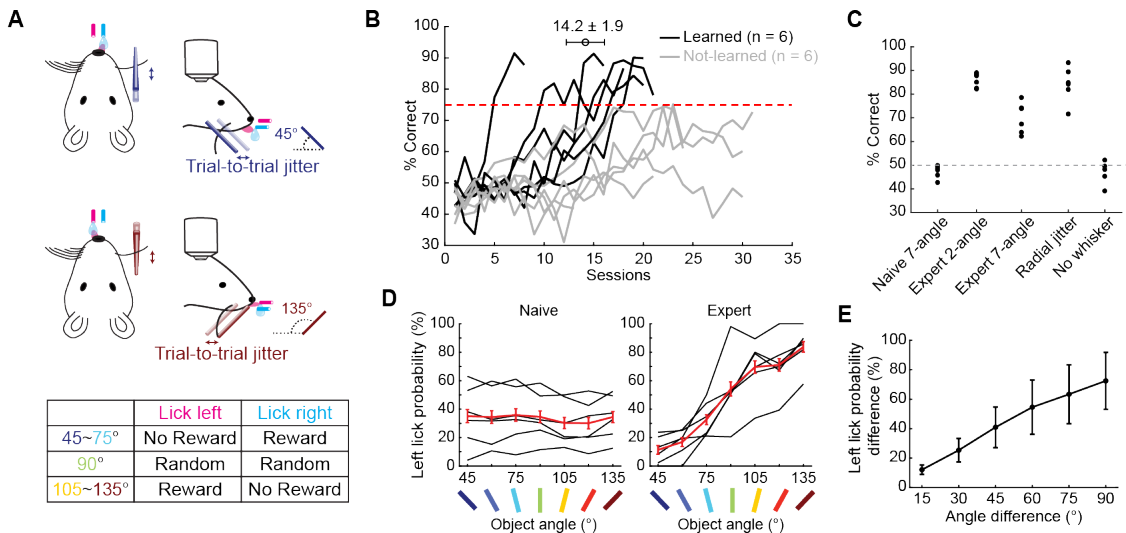


**Figure 1.** Two-choice object-angle discrimination task.

(A) Task design (top) and contingency table of object angle and rewarded side (bottom). Pole-shaped object rotated in the sagittal plane parallel to the body axis of mice. Object angle was defined respective to the horizontal plane in caudal direction, clockwise when looking at the animal from the right side. There was 1-2 mm anteroposterior trial-to-trial jitter.

(B) Learning curves of all 12 mice. Six mice ("Learned") crossed 75% correct rate (red dotted line) over 3 consecutive sessions starting at  $14.2 \pm 1.9$  (mean  $\pm$  SEM.) sessions.

(C) Performance of learned mice at different training sessions (n = 6).

(D) Left lick probability in 7-angle sessions, before and after learning. Black: individual learned mice. Red: Mean  $\pm$  SEM.

(E) Difference in left lick probability plotted against difference in the object angle, in expert 7-angle sessions. (n = 6; Mean  $\pm$  SD.)

**Figure 2**

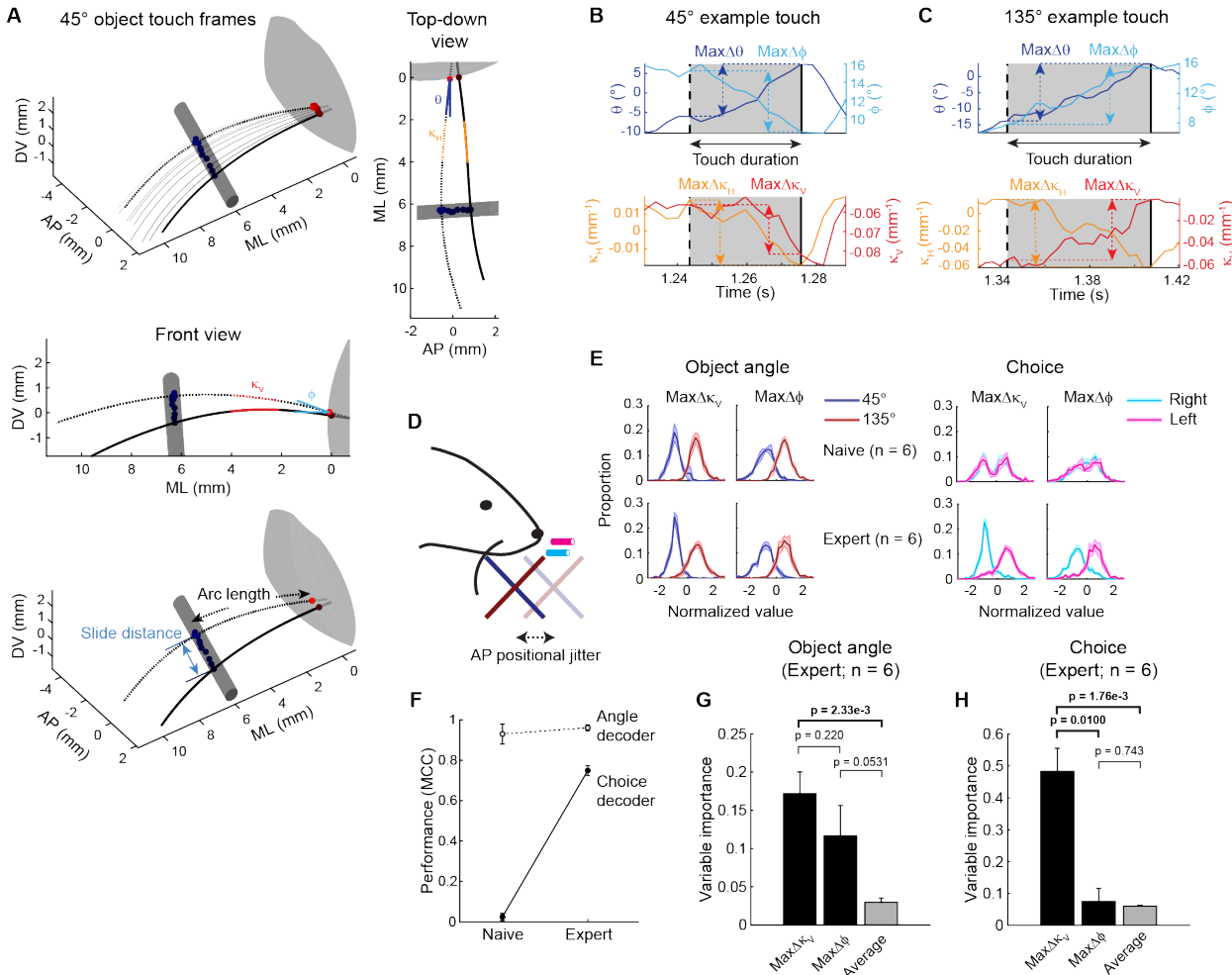


**Figure 2.** Whisker-object interaction features for choice.

(A) Example of frame-by-frame 3D-reconstructed whiskers during a single protraction touch. Whisker at the first frame of touch is shown in dotted black curves, and that of the last frame is shown in solid black curves (matched in (B) and (C)). Whisker base points (red), whisker-object contact points (blue), and whisker shapes (light grays) are gradually darkened in color to represent frame progression. Horizontal whisker base angle ( $\theta$ ) and curvature ( $\kappa_H$ ) are described in top-down view (right), vertical whisker base angle ( $\phi$ ) and curvature ( $\kappa_V$ ) in front view (middle), and arc length and slide distance in 3D view (bottom). Dark gray pole-shape: the object (45° in this example); gray convex patch on the right: face mask. DV: dorsoventral. AP: anteroposterior. ML: mediolateral. Zero values were defined by the averaged whisker base points of this trial.

(B) Example graphs describing the calculation of maximum change in azimuthal angle (max $\Delta\theta$ ; blue), maximum change in elevation angle (max $\Delta\phi$ ; cyan), maximum change in horizontal curvature (max $\Delta\kappa_H$ ; orange), maximum change in vertical curvature (max $\Delta\kappa_V$ ; red), and time spent touching object during a protracting whisk (touch duration; gray background), during a 45° object touch. Vertical dashed and solid black lines: first and last time points of this protraction touch, respectively.

(C) Same as in (B), but during a 135° object touch.

(D) Object-angle and choice decoding was examined in 2-angle sessions, using 45° and 135° objects.

(E) Distributions of max $\Delta\kappa_V$  and max $\Delta\phi$  when grouped by angles (left) in naive (top) and expert (bottom) sessions, and when grouped by choices (right).

(F) Performances (MCC: Mathew's correlation coefficient) of binomial GLM angle decoder and choice decoder.

(G) Variable importance of max $\Delta\kappa_V$  and max $\Delta\phi$  compared to average single features from the binomial GLM angle decoder.

(H) Same as in (G) but from the choice decoder.

All error bars represent mean  $\pm$  SEM. from  $n = 6$  mice. P-values are from uncorrected multiple paired *t*-test.

**Figure 3**

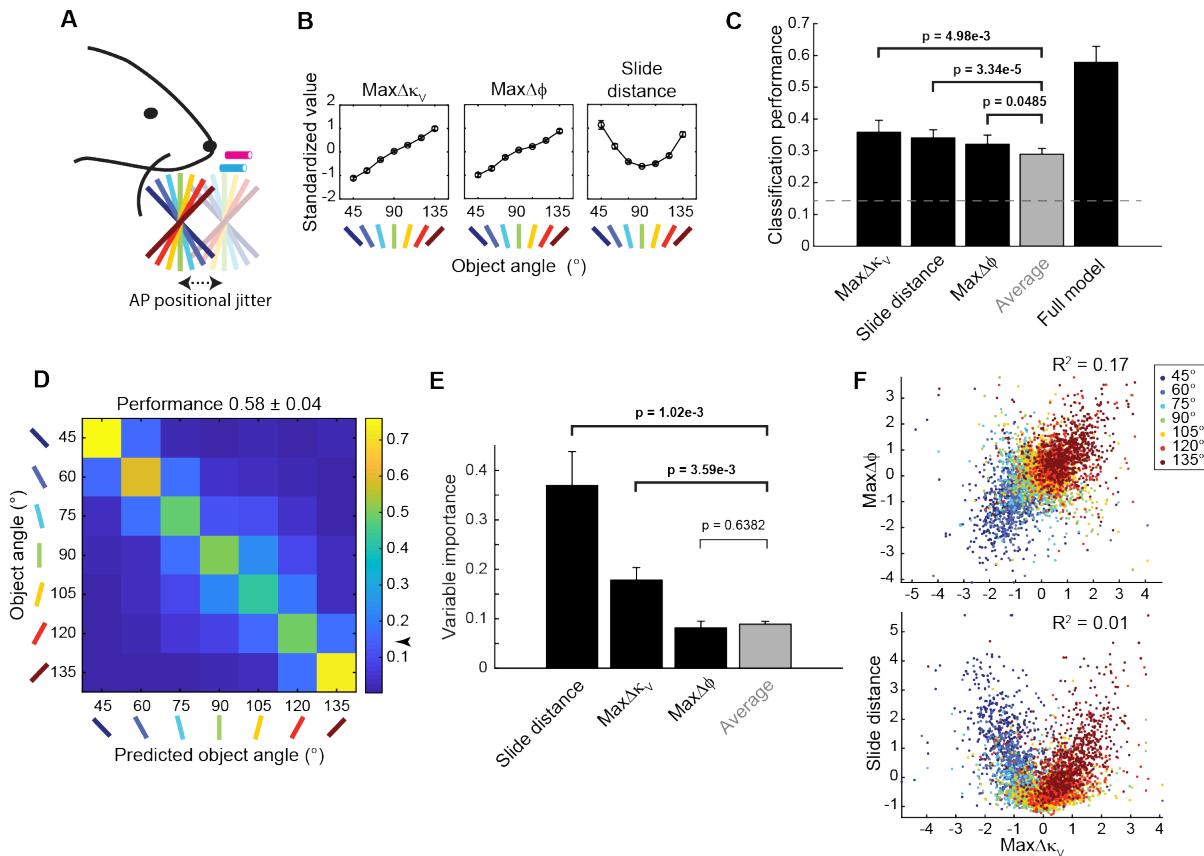


**Figure 3.** Vertical bending and slide distance are the most important whisker-object interaction features in fine angle discrimination.

(A) Fine object-angle decoding was examined in 7-angle sessions, using objects angled at 45° to 135° in 15° interval.

(B) Standardized values of  $\text{max}\Delta\kappa_V$ ,  $\text{max}\Delta\phi$ , and slide distance plotted against object angles.

(C) Classification performance of multinomial GLMs from top 3 whisker features compared to average performance of all whisker features, when each feature was used alone. Performance of a multinomial GLM using all 12 whisker features were shown for comparison ('full model', same as in (D)). Gray dashed line: chance level.

(D) Contingency matrix of the full model. Chance level is shown on the right (arrowhead).

(E) Variable importance of  $\text{max}\Delta\kappa_V$ ,  $\text{max}\Delta\phi$ , and slide distance in full model, compared to average of all features.

(F) Scatter plots of standardized values of  $\text{max}\Delta\phi$  (top) and slide distance (bottom) against  $\text{max}\Delta\kappa_V$  from all trials across mice.

All error bars and numbers represent mean  $\pm$  SEM. from n = 12 naive mice. P-values are from uncorrected multiple paired t-test.

**Figure 4**

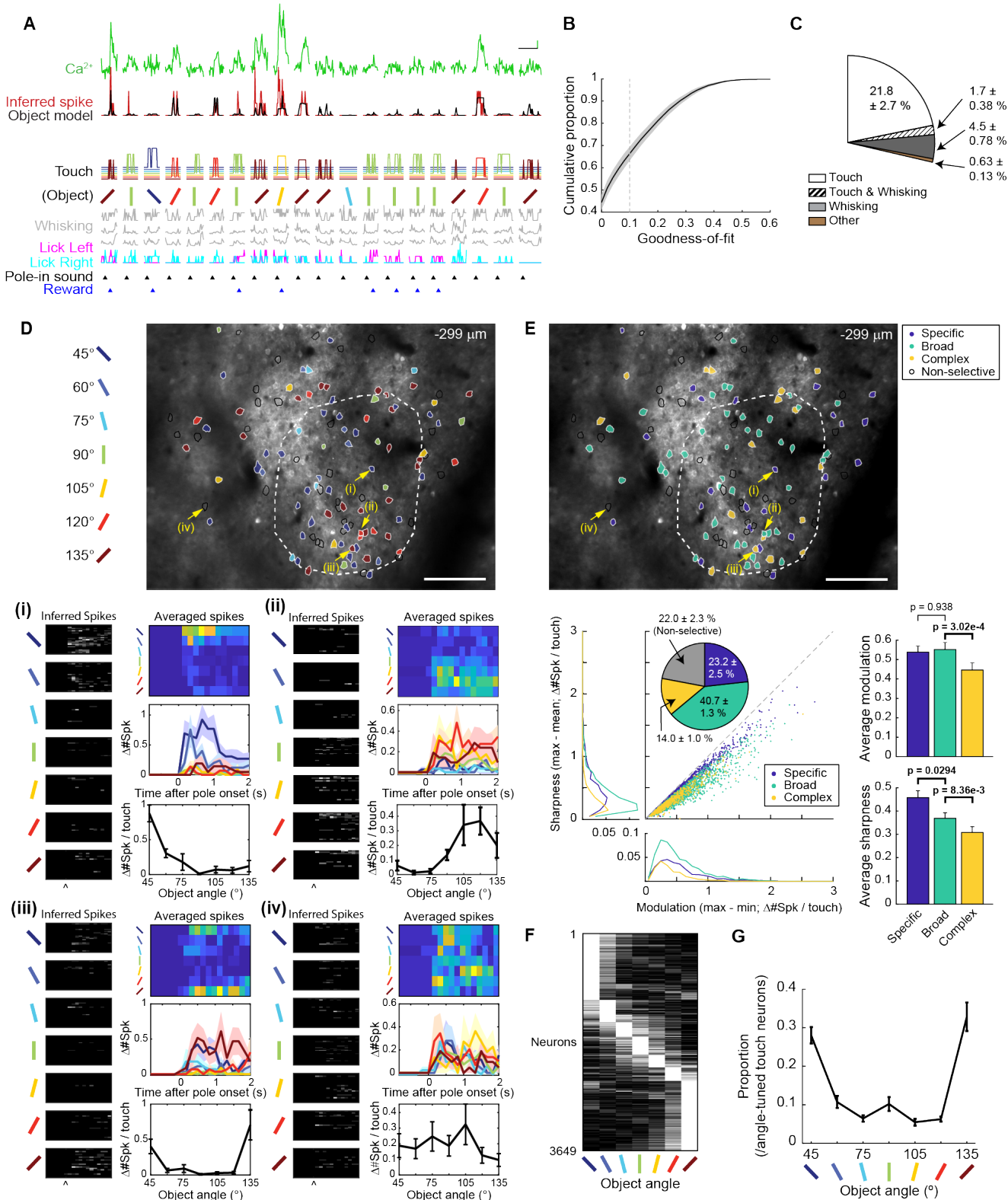


**Figure 4.** Angle-tuned touch-responsive excitatory neurons are distributed across L2-L4 barrel cortex.

(A) Example traces for 'object model' explanation. Traces are divided by trials. Temporal delays (**Methods**) were omitted for clarity. One input from touch parameters were omitted (all touch; see **Methods**). Whisking parameters (gray) were number of whisks (top), amplitude (middle), and midpoint (bottom). Goodness-of-fit of this example was 0.2194. Scale bars: black, 5 s; green, 1  $\Delta\text{F/F}_0$ .

(B) Distribution of goodness-of-fit of 'object model' from all naive mice. Vertical dashed gray line indicates the threshold.

(C) Average proportion of event classes assigned to each neuron ( $n = 12$ ). 'Other' represents licking, sound, and reward combined. Intersection of these 'other' categories with either whisking or touch were disregarded.

(D) Example field-of-view (FOV) of two-photon calcium imaging. All region-of-interests representing touch-responsive neurons were overlaid. Maximally preferred angle of angle-tuned neurons were color-coded as shown on the left. Non-selective neurons were shown

with black boundaries. White dashed line represents C2 column boundary. Scale bar, 100  $\mu$ m. (Di) An example of specific-tuned neuron (yellow arrow in (D)). Inferred spikes from all trials grouped by the angle of presented object (left; arrowhead on the bottom represents pole onset time point), a normalized heat map (right top) and time series graphs (right middle) of average response in number of inferred spikes from each angle, and average response in number of inferred spikes per touch grouped by object angle (right bottom). (Dii) Same as in (Di) but for a broad-tuned example neuron. Same example neuron shown in (A) and **Figure 5A**. (Diii) Same as in (Di) but for a complex-tuned example neuron. (Div) Same as in (Di) but for a non-selective example neuron.

(E) (Top) Example map of angle tuning types in the same FOV as in (D). (Bottom) Scatter plot of sharpness vs modulation in angle-tuned neurons (left), distribution of types of angle tuning (left inset), average modulation (right top; repeated ANOVA,  $F_{2,22} = 14.9$ ,  $p = 8.15e-5$  with Greenhouse-Geisser adjustment), and average sharpness (right bottom; repeated ANOVA,  $F_{2,22} = 5.22$ ,  $p = 0.0316$  with Greenhouse-Geisser adjustment) across different types of angle-tuning. P-values are from multiple comparison using Tukey-Kramer procedure.

(F) Normalized activity of all angle-tuned neurons ( $n = 3127$ ) from all 12 naive mice, sorted by maximally preferred angles from 45° to 135°.

(G) Distribution of maximally preferred angles plotted against object angle.

All error bars, shaded area, and pie chart numbers represent mean  $\pm$  SEM. ( $n = 12$ ).

**Figure 5**

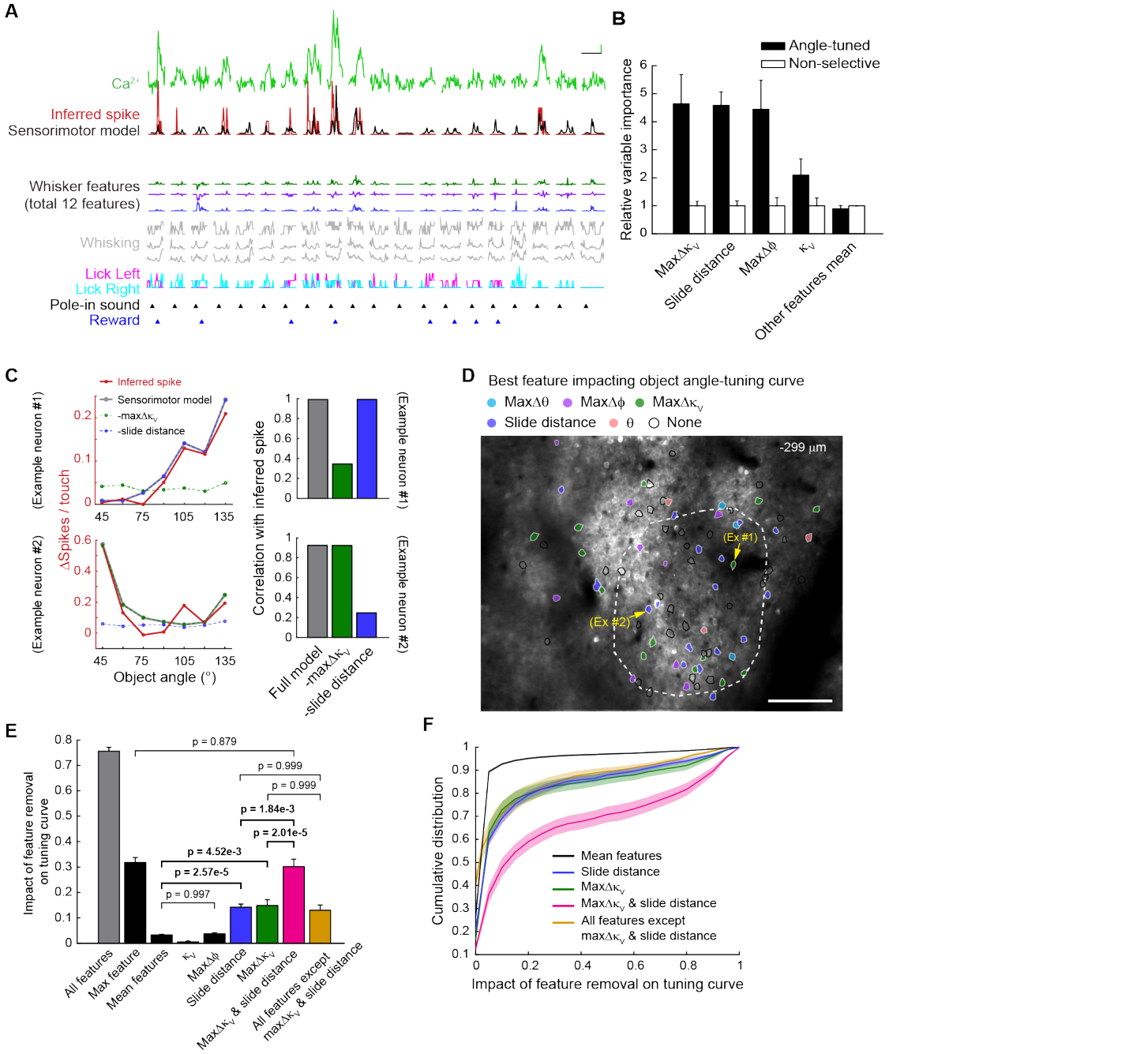


**Figure 5.** Vertical bending and slide distance best explain angle-tuning curves of S1 excitatory neurons.

(A) Example traces for 'sensorimotor model' explanation. Same neuron and same trials as shown in **Figure 4A**, with touch inputs swapped with whisker features (tactile input). Only 3 whisker features out of 12 were shown for clarity:  $\text{max}\Delta\kappa_v$  (green),  $\text{max}\Delta\phi$  (purple), and slide distance (blue). Scale bars: black, 5 s; green,  $1 \Delta F/F_0$ .

(B) Relative variable importance of candidate sensorimotor features selected by having statistically significantly higher variable importance in 'sensorimotor model' of angle-tuned neurons compared to that of non-selective neurons ( $p < 0.05$  from paired  $t$ -test). Variable importance values are divided by the mean of those in non-selective neurons.

(C) Example graphs for calculation of impact on angle tuning. (Left) Average response in each object angle from inferred spikes (red), full 'sensorimotor model' (gray),  $\text{max}\Delta\kappa_v$  'leave-one-out' model (dashed green), and slide distance 'leave-one-out' model (dashed blue). Response values of models are normalized to match inferred spike response. (Right) Angle-tuning curve correlation between each model and inferred spikes. (Top) An example angle-tuned neuron of which the angle tuning was affected by  $\text{max}\Delta\kappa_v$ . (Bottom) An example angle-tuned neuron of which the angle tuning was affected by slide distance. Both example neurons are mapped in (D). (D) An example map of whisker features that impacted angle tuning the most in each neuron, with the impact value at least 0.1 (otherwise marked as none). Example neurons match with (C).

(E) Impact of feature removal on angle-tuning curves. (One-way repeated ANOVA between max feature, mean features,  $\kappa_V$ ,  $\max\Delta\varphi$ , slide distance,  $\max\Delta\kappa_V$ , slide distance &  $\max\Delta\kappa_V$ , and all features combined except  $\max\Delta\kappa_V$  & slide distance;  $F_{7,77} = 57.021$ ,  $p = 9.37e-9$  with Greenhouse-Geisser adjustment; p-values are from post hoc analysis using Tukey-Kramer procedure.)

(F) Cumulative distribution of the impact on angle-tuning curves in each model. Impact values can be negative when removing features increased the angle-tuning curve correlation.

All data are shown in mean  $\pm$  SEM. (n = 12).

**Figure 6**

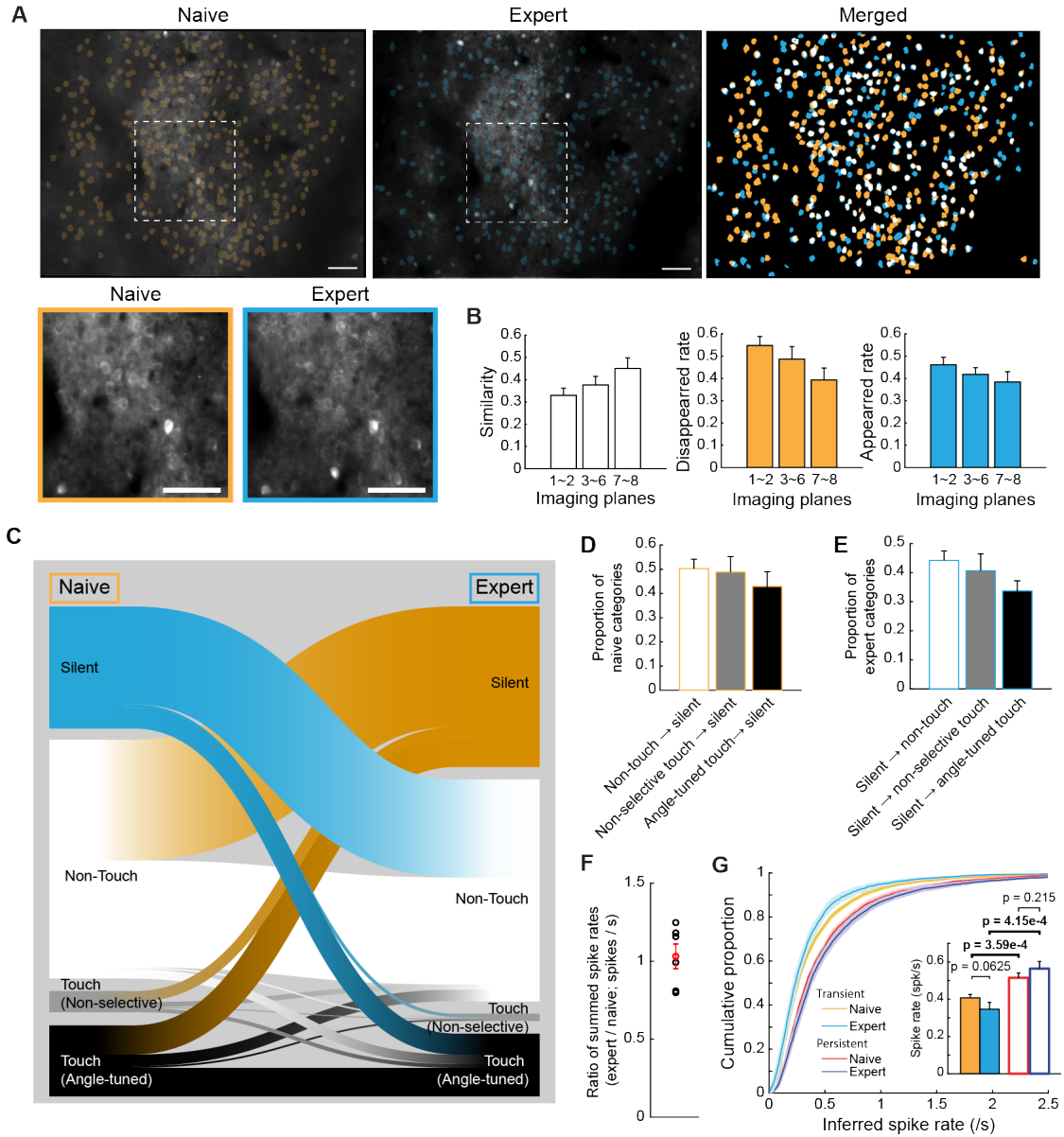


**Figure 6.** Active ensemble membership exhibits high turnover across learning.

(A) Example field-of-view (FOV; same as in **Figure 4**) before (left) and after (middle) learning. Yellow patches represent region-of-interests (ROI's) in naive 7-angle session, and cyan patches represent ROI's in expert 7-angle session. Right shows both before and after learning, with overlap regions shown in white. Bottom shows magnified FOV between naive and expert sessions (white dashed square region in top). Scale bars: 100  $\mu$ m (top), 50  $\mu$ m (bottom).

(B) Similarity, disappeared rate, and appeared rate in different imaging planes.

(C) A Sankey plot of all 11,351 neurons in 6 mice from naive to expert 7-angle session.

(D) Proportion of naive neurons in each category fell silent after learning.

(E) Proportion of expert neurons in each category that were silent before learning.

(F) Summed spike rates of all neurons in expert sessions divided by those in naive sessions within each mouse. Black circle: mouse; red: mean  $\pm$  SEM.  $p = 0.716$ , t-test  $H_0$ : mean = 1.

(G) Mean inferred spike rates in transient and persistent neurons.

All error bars represent mean  $\pm$  SEM. ( $n = 6$ ).

**Figure 7**

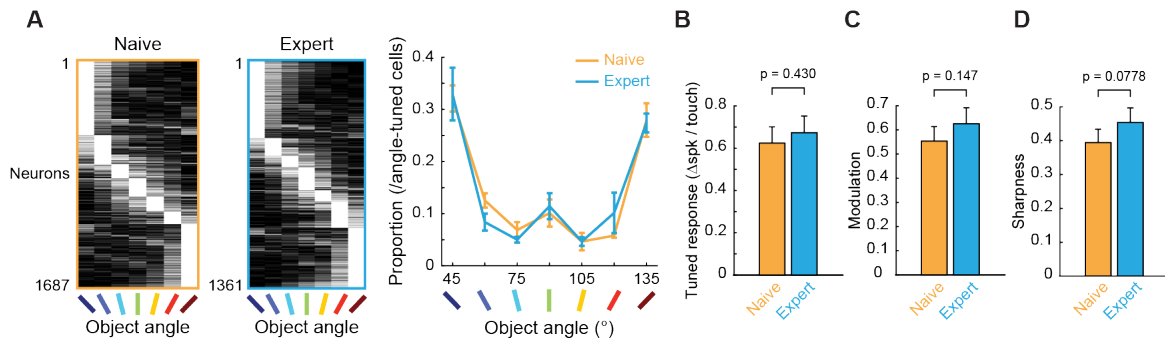


**Figure 7.** Population distribution of angle tuning is stable across learning.

(A) (Left) Normalized activity of all angle-tuned neurons from 6 learned mice in naive and expert 7-angle sessions, sorted by maximally preferred angles from 45° to 135°. (Right) Distribution of maximally preferred angles in naive and expert mice.

(B) Mean response to maximally preferred angle of angle-tuned neurons in naive and expert sessions.

(C) Tuning modulation depth of angle-tuned neurons in naive and expert sessions.

(D) Tuning sharpness of angle-tuned neurons in naive and expert sessions.

All error bars represent mean  $\pm$  SEM. (n = 6). P-values are from paired *t*-test.

**Figure 8**

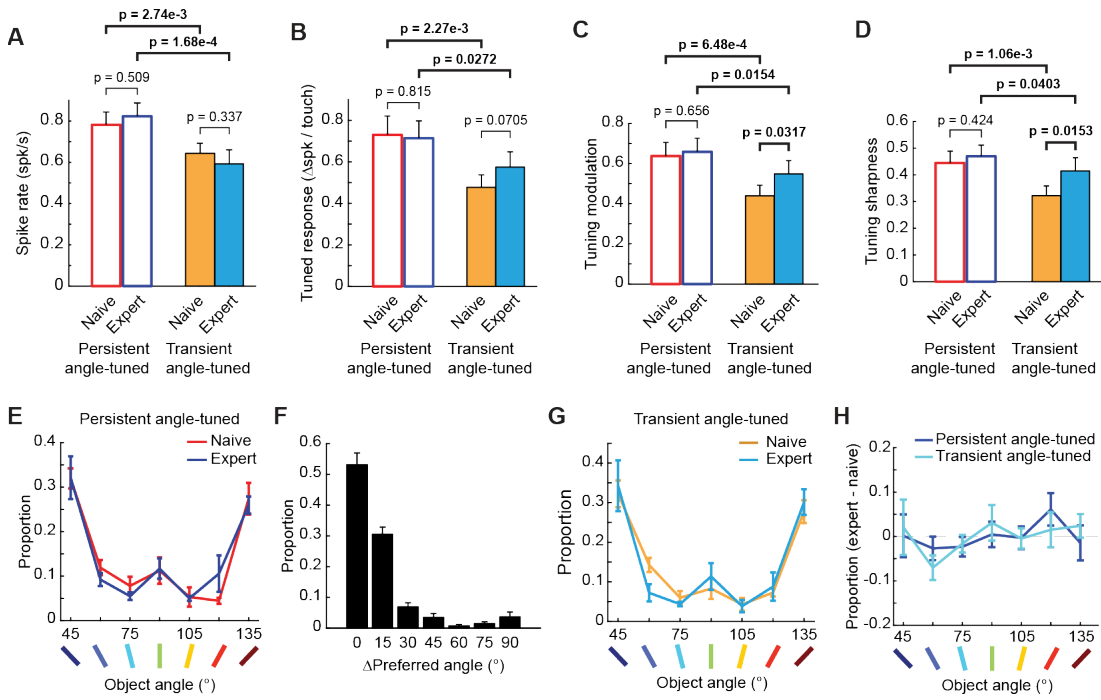


**Figure 8.** Stable tuning properties in persistent angle-tuned neurons with sharper tuning in transient angle-tuned neurons after learning.

(A) Mean inferred spike rates in persistent and transient angle-tuned neurons.

(B) Mean response to maximally preferred object angle in persistent and transient angle-tuned neurons.

(C) Tuning modulation depth in persistent and transient angle-tuned neurons.

(D) Tuning sharpness in persistent and transient angle-tuned neurons.

(E) Distribution of maximally preferred angle in persistent angle-tuned neurons, before and after learning.

(F) Distribution of change in maximally preferred angle in persistent angle-tuned neurons after learning.

(G) Distribution of maximally preferred angle in transient angle-tuned neurons, before and after learning.

(H) Difference in distribution of maximally preferred angle between expert and naive sessions, in persistent (one-way ANOVA,  $F_{6,35} = 0.771$ ,  $p = 0.598$ ;  $t$ -test of all values to 0 mean,  $p = 1.00$ ) and transient (one-way ANOVA,  $F_{6,35} = 0.916$ ,  $p = 0.495$ ;  $t$ -test of all values to 0 mean,  $p = 1.00$ ) angle-tuned neurons.

All graphs are shown in mean  $\pm$  SEM ( $n = 6$  mice). P-values are from uncorrected multiple paired  $t$ -test.